Review of
Scientific Instruments

ARTICLE

pubs.aip.org/aip/rsi

Indigenous facility of the unipolar pulsed power generation for gas flow sputtering of titania films

Cite as: Rev. Sci. Instrum. 94, 075104 (2023); doi: 10.1063/5.0148807
Submitted: 2 March 2023 • Accepted: 22 June 2023 •
Published Online: 12 July 2023

View Online Export Citation CrossMark

Nivin Alktash,[1,a)] **Ruslan Muydinov,**[1,a)] **Darja Erfurt,**[2] **Manuel Hartig,**[1,2] **Wojciech Gajewski,**[3] **and Bernd Szyszka**[1]

AFFILIATIONS

[1] Institute for Semiconductor- and High-Frequency-System Technologies, Technical University Berlin, Einsteinufer 25, 10587 Berlin, Germany
[2] PVcomB, Helmholtz-Zentrum für Materialien und Energy GmbH, Berlin, Schwarzschildstraße 3, 12489 Berlin, Germany
[3] TRUMPF Huettinger Sp. z o.o., Marecka 47, Zielonka 05-220, Poland

[a)] **Authors to whom correspondence should be addressed:** alktash@tu-berlin.de and ruslan.muydinov@campus.tu-berlin.de

ABSTRACT

Gas flow sputtering is a sputter deposition method that enables soft and high-rate deposition even for oxides or nitrides at high pressure (in the mbar range). A unipolar pulse generator with adjustable reverse voltage was used to optimize thin film growth by the hollow cathode gas flow sputtering system. In this regard, we describe our laboratory Gas Flow Sputtering (GFS) deposition system, which has been recently assembled at the Technical University of Berlin. Its technical facilities and suitability for various technological tasks are explored. The first experimental efforts are presented by the example of TiO_x films on glass substrates obtained at various deposition conditions with forced Argon flow. The influence of pulsing parameters, power, and oxygen gas flow on the plasma generated is studied. The films were characterized by ellipsometry, scanning electron microscopy, x-ray diffraction, and x-ray reflectivity. Optical Emission Spectroscopy (OES) was also used to characterize the remote plasma, and the substrate temperature was measured. The pulsing frequency (f) is a significant factor that provides additional substrate heating by about 100 °C when the plasma regime changes from $f = 0$ (DC) to 100 kHz. Such a change in frequency provides a significant increase in the OES signals of Ti and Ar neutrals as well as of Ti^+ ions. With pulsed operation at high power, the GFS plasma is capable of heating the glass substrate to more than 400 °C within several minutes, which allows for crystalline anatase TiO_x film deposition without external heating. For deposition below 200 °C substrate temperature, low power DC operation can be used.

I. INTRODUCTION

The hollow cathode discharge has been known since 1916, when Paschen investigated it as a UV-light source and found that the thus generated plasma is characterized by high electron flux and low temperatures of neutrals and ions.[1] Later, this technology was used for the activation of evaporation and, finally, as a sputtering deposition technique.[2] Gas Flow Sputtering (GFS) has been intensively developed since the 1980s by several groups in parallel. Special attention has been drawn to this technique owing to the high ionization degree of plasma and, at the same time, the low energy of its species. These factors together secure high deposition rates under soft growth conditions.[3,4] Compared to magnetron sputtering, GFS has the following advantages: (i) low process vacuum in the mbar range and, consequently, cheaper machinery; (ii) stable reactive process due to spatial separation of sputtering and reactive gases; and (iii) relative compositional freedom (variable doping, magnetic materials, gradient oxynitrides, complex oxides as delafossites, and composite films). Additionally, this method combines physical vapor deposition (PVD) and plasma enhanced chemical vapor deposition (PECVD) processes in a single system that allows the *in situ* production of nanocomposite thin films.[5] A thorough investigation of titania nanocomposite films for photocatalytic applications was the subject of the European project NANOHAP several years ago.[6] Titania films deposited by various sputtering techniques were investigated and evaluated extensively over the years.[7–11] In this sense, it is a good material to compare and assess any different or modified approach to sputtering. The GFS method, with its high deposition rate and thermalized state of plasma, usually results in films with insufficient optical application density but useful catalytic porosity. The use of reverse (positive) voltage (U_{rev}) pulses can decrease the negative charging of the substrate surface and provide intensive, low energetic ion bombardment, which enhances diffusion. In this work, we investigated how variable reverse voltage influences the microstructure, crystallinity, and optical properties of titania films. Our small GFS system is equipped with the modern 10 kW TruPlasma power generators (Hüttinger GmbH), which allow us to set U_{rev} from 0 to +100 V with a frequency up to 100 kHz and a pulse time of 2 μs. Optical emission spectroscopy (OES) analysis was also performed to characterize different plasma conditions and engage these data with the properties of titania films.

II. DESCRIPTION OF THE GFS SYSTEM

Figure 1 shows the opened vacuum chamber (75.3 dm^3 in volume and 55 cm in diameter) of the GFS deposition system used in this work.

The substrate holder has an argon gas supply (behind) and a coaxial reactive gas inlet (in front); see also Fig. 11. Tubular targets have a 60 mm length, a 50 mm outer diameter, and a 40 mm inner diameter. It must be conductive, in the simplest case—metallic, which is far more affordable in such a form than ceramic ones. Therefore, in most cases, the deposition of oxides requires a reactive process. The inlet of reactive gas is outside the sputter-source (see Fig. 11), which prevents interaction with the target surface if a high enough argon flow is ensured. Our system has the following choice of reactive gases: O_2, N_2, and the forming gas Ar/H_2. This choice allows depositing oxygen free metal films, oxides with variable oxygen stoichiometry, oxynitrides, nitrides, and films with gradient composition. The reactive gas may also be used as a carrier for the desirable admixing of suitable vapors. In this way, a water vessel is connected via a needle valve to the oxygen line to obtain films of such materials as In_2O_3:H (IOH).[12] Another available option in our GFS system is the precise feeding of, e.g., tetramethylsilane (TMS) vapors. The decomposition of this compound in the reactive zone may provide Si-doping or the incorporation of Si/SiO_x nanoparticles into the depositing films, increasing their resistance to corrosion.[13–15] Moreover, the target may be assembled from different segments. In this way, doped or complex oxides as well as composite films can be deposited. For example, ten small, 0.1 mm thick rings correspond to ~1.8 % impurity incorporation at the same sputtering rate.[16] These features enable exceptional compositional freedom.

The substrate holder is movable, which enables execution of (i) substrate pre-treatment in the pre-treatment section and Ar pre-sputtering for target conditioning; and (ii) deposition in stationary or dynamic oscillating regimes. Substrate pre-treatment may include (i) heating from both sides (back and front) and (ii) plasma etching by applying a bias voltage to the substrate holder. In both cases, various gases (Ar, N_2, O_2, and Ar/H_2) can be fed through the pre-treatment section. Two temperature-controlled heating units are used for substrate heating. One unit is placed behind the substrate on the substrate holder, and a second unit is placed in the pre-treatment station to enable both-side substrate heating. Before deposition, the substrate-to-source (d_{st}) distance can be set in the range of 1.5, . . ., and 4.5 cm by positioning the sputter source. A variation of other deposition parameters is given in Fig. 1(b).

Real-time control of the hardware components, setting of the deposition parameters, and creation of the process recipes are conducted using a programmable logic controller-based control cabinet (GHS Prozeßautomation GmbH[17]). The communication between

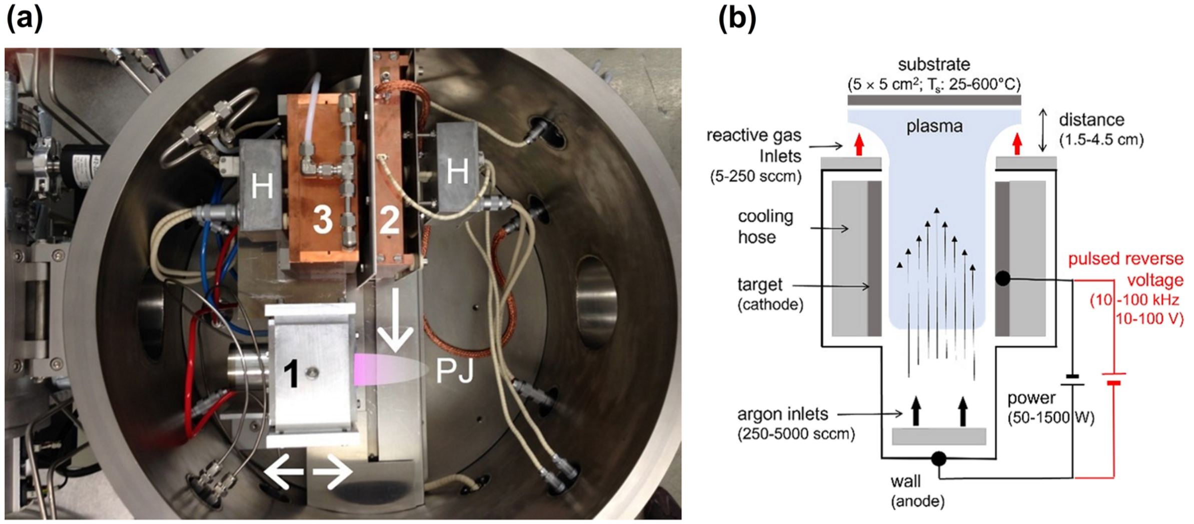

FIG. 1. (a) Top-view photo of the GFS deposition chamber with the following main units: 1—sputter-source with the tubular target inside; 2—linearly movable (path is shown by an arrow) substrate holder; and 3—treatment station with gas supply and splitter. The letters "H" denote the infrared heating units, and the "PJ" points at a painted plasma jet, representing its approximate look. Sputter-sources can be set at different distances from the substrate holder, as shown by a double arrow. (b) Schematic representation of the GFS deposition process in cross-section.

hardware and software occurs via PROFIBUS,[18] which works as a parallel rail. A baud rate in this case does not allow detecting and managing arc-events on a sub-microsecond scale. A special arc-management routine patented (EP2026376A) by Hüttinger GmbH is realized via the PVD-Power software, which includes a digital oscilloscope and trend features. Two unique features, namely variable reverse voltage, adjusted to 100 V, and complex arc recognition, are shown in Fig. 2.

Setting the reverse voltage (U_{rev}) for a short moment relieves the positive charging of the target. Furthermore, the ion bombardment of the substrate is enhanced during such an operation. This enhances, in turn, the range of set parameters within which the process remains stable.

Arc recognition occurs in three possible routines. The current-based detection reacts when the output current exceeds the user-defined $I_{\max}$-threshold. The dU-detector works when the output voltage starts falling faster than the user-defined voltage change. And finally, the cross $U \times I$ observation of voltage and current acts when either output voltage or current goes beyond the user-defined thresholds.

Once an arc has been detected, the output power is switched off. At the same moment, the time controller and the break time counter are initiated. After a break, the shut-down signal is released, and output power returns to its previous setting value with a ramp, which is programmable. The detection time is assuredly less than 100 ns, and the switch-off time does not exceed 300 ns. Usually, at an arc-accident, the output voltage drops much faster than the output current increases, which is why the dU criterion allows detecting arcs at a very early stage. As a result, powerful arc-management allows for the stability of the deposition process even with the steady occurrence of micro-arcs.

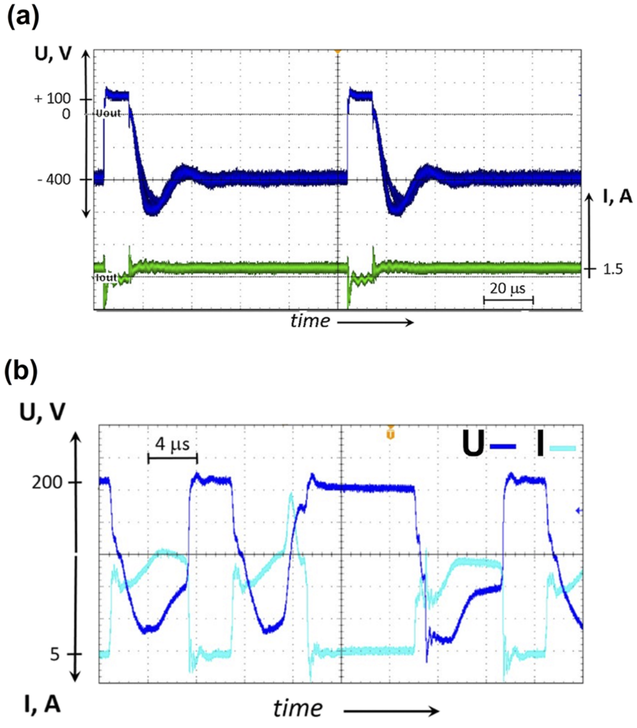

FIG. 2. Unique features of the TruPlasma power supply: (a) example of an adjustable reverse voltage in a pulse-mode: reverse (positive) voltage U_{rev} = 100 V, frequency f = 10 kHz, and pulse time τ = 10 μs; and (b) arc-detection and handling at DC operation, dU criterion alarm. The plots are printed from the digital oscillography screens and adopted.

III. INVESTIGATION OF THE GFS PLASMA

Our deposition process may be presented as shown in Fig. 1(b), where a glow discharge with a high plasma density appears inside the tubular hollow cathode (target) as a result of applying a negative voltage to it. Langmuir probe measurements revealed plasma density in the order of 10^{12} cm^{-3} at the substrate position.[19] Sputtered atoms are transported from the inner surface to the remote substrate with laminar argon flow. At the outlet, the pressure drops, and a stagnation point over the substrate is created. Grazing flow over the substrate forms a diffusion layer with a stable concentration gradient for the species being deposited. High process pressure (mbar range) stipulates small mean free path values (mm range) for the gas species. Multiple collisions provide high ionization and thermalization degrees in the GFS plasma. A reactive gas can be added outside the hollow cathode and react at the substrate surface with the sputtered material. More details on the ranges of deposition parameters are shown in the figure. The plasma parameters [p_{tot} = 0.34 mbar, q(Ar) = 1000 SCCM, and q(O_2) = 80 SCCM] for titania films were chosen based on previous expertise.[5,20,21]

A. Heating of the substrate surface by GFS plasma

Since thermalized GFS plasma may transform thermal energy into a substrate, we estimated its impact. No intentional heating was used. In our work, substrate temperature (T_s) was measured using the thermal profiler SuperM.O.L.E.® Gold 2 (Electronic Controls Design, Inc., USA). Three type K thermocouples were sequentially placed on a substrate as shown in Fig. 12(b) and measured T_s in parallel. The thermocouples were fixed using special thermal grease.[22] Since the temperature steadily increased during the first deposition minutes [Fig. 12(a)], its value was fixed 6 min after plasma ignition. Figure 3 shows T_s measured depending on plasma conditions and glass thickness for two different discharge powers. Two different glass types were taken: 3.1 mm thick low-iron soda lime glass type Diamant (Saint-Gobain Glass, Germany) and 0.7 mm thick borosilicate glass Eagle XG (Corning, USA). As one can see, higher discharge power causes a higher surface temperature. Thinner glass is heated to generally higher surface temperatures. A high pulsing frequency is a factor in providing a stronger thermal impact. This circumstance is also known in the literature.[19]

The temperature of the substrate surface determines lateral diffusion during deposition, which in turn depends on plasma conditions (total pressure, power generation).

Heat accumulates on the surface via (1) condensing particles transferring both kinetic and potential energy; (2) bombarding species (ions, electrons, and neutral atoms); and (3) positive ions recombining with electrons at the surface.[23–27]

As shown in Fig. 12(a), substrate temperature increases rapidly after the ignition of plasma and, after several minutes, approaches a limit that corresponds to thermal equilibrium. The temperatures in Fig. 3 were measured after 6 min of exposure to the GFS plasma.

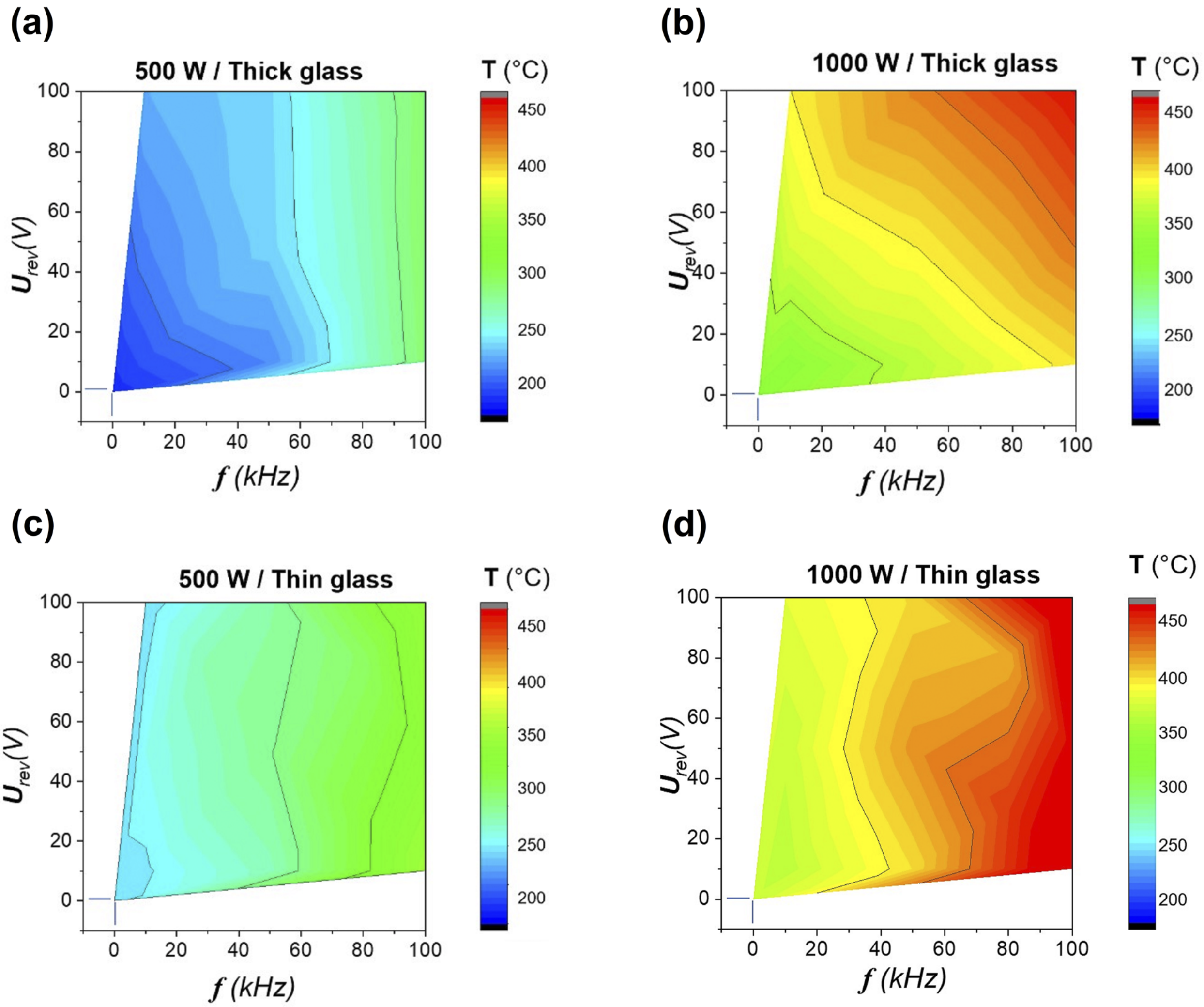

FIG. 3. Glass surface temperature in the middle of a substrate depends on the power [(a) and (c)—500 W; (b) and (d)—1000 W], pulsing conditions [DC regime corresponds to (0; 0)], and glass thickness [(a) and (b)—3.1 mm; (c) and (d)—0.7 mm]. Each T-surface was displayed based on 14 (one at DC and 13 at plasma conditions) measurement points. For deposition, titanium target with q(Ar) = 1000 SCCM, q(O_2) = 80 SCCM, and p_{dep} = 0.34 mbar have been used.

The measured temperatures will most probably differ from the ones on the real surface due to the difference in emissivity between glass and metal. Still, the gathered values reproduced a difference in plasma impact itself, especially in cases of more conductive and thick films (Fig. 3). As one can see, temperatures may vary from ~150 °C to more than 450 °C depending on plasma conditions. In a balanced magnetron plasma, relatively low substrate heating is explained by the confinement of the secondary electrons and ions close to the target.[28] An unbalanced magnetron plasma heats substrates more due to the bombardment of the surface by neutral particles and fast electrons.[19,29,30] Still, substrates are usually placed far away from the target in those processes, and the thermal impact is low. In addition, the process pressure in magnetron sputtering (MS) is about two orders of magnitude lower than in GFS. Finally, an impingement rate (Z) for plasma species is outstanding in the latter case,

$$z = \frac{P}{\sqrt{2\pi mkT}},$$

where P is the gas pressure, m is the particle mass, k is Boltzmann's constant, and T is the temperature (kinetic energy).[24] This, in combination with the transport of plasma (see Figs. 1 and 11) to the very surface of a substrate, secures far more effective energy transfer as compared to any other low pressure sputtering technique.[24,31]

Recombination of the ion-electron pairs at the substrate surface and convective substrate heating are the major mechanisms of substrate heating by plasma. In the recombination of an ion-electron pair, a third body is needed to conserve energy and momentum after recombination. In a gas phase, threefold collisions are unlikely and, hence, very rare. In contrast, collisions with any surface (substrate or wall) represent the predominant mechanism of plasma energy losses. According to Kaelber, about 90% of the recombination energy is transferred to the substrate via such collisions.[19] Convection also plays a significant role since the “fresh” plasma is constantly delivered to the substrate with a gas flow [q(Ar) = 1000 SCCM] and a corresponding speed exceeding 1 cm/s.

Radial gas distribution over the substrate stipulates deceleration of the flow. At the same time, plasma energy dissipates. This all suggests a lower T at the substrate edge compared to its center, right in front of the plasma source outlet. We measured the difference (ΔT) between the temperature in the middle of a substrate and the average one for the side points [see Fig. 12(b)]. At 500 W DC power, ΔT was found to be around 20 °C for the thick glass and ~50 °C for the thin one. When DC power increases from 500 to 1000 W, ΔT rises for both substrates by about 10 °C. In a pulsed regime, ΔT gets

TABLE I. The electronic state configurations, wavelengths, and energies of the upper and lower states of the emission lines are studied in this paper.

Species	Wavelength (nm)	Energy levels ($E_k - E_i$)	Configurations
Argon I	367.52	15.2–11.82	$3s^23p^5(^2P_{1/2})6p-3s^23p^5(^2P_{1/2})4s$
Argon I	419.83	14.58–11.62	$3s^23p^5(^2P_{3/2})5p-3s^23p^5(^2P_{3/2})4s$
Argon I	464.75	15.57–12.91	$3s^23p^5(^2P_{3/2})9d-3s^23p^5(^2P_{3/2})4p$
Argon I	696.54	13.33–11.55	$3s^23p^5(^2P_{1/2})4p-3s^23p^5(^2P_{3/2})4s$
Argon I	706.72	13.30–11.54	$3s^23p^5(^2P_{1/2})4p-3s^23p^5(^2P_{3/2})4s$
Argon I	737.21	14.76–13.08	$3s^23p^5(^2P_{3/2})4d-3s^23p^5(^2P_{3/2})4p$
Argon I	750.39	13.48–11.83	$3s^23p^5(^2P_{1/2})4p-3s^23p^5(^2P_{1/2})4s$
Argon I	762.89	14.95–13.33	$3s^23p^5(^2P_{1/2})4d-3s^23p^5(^2P_{1/2})4p$
Argon I	772.38	13.15–11.54	$3s^23p^5(^2P_{3/2})4p-3s^23p^5(^2P_{3/2})4s$
Argon I	800.62	13.17–11.62	$3s^23p^5(^2P_{3/2})4p-3s^23p^5(^2P_{3/2})4s$
Argon I	810.37	13.15–11.62	$3s^23p^5(^2P_{3/2})4p-3s^23p^5(^2P_{3/2})4s$
Argon II	410,39	22.51–19.49	$3s^23p^4(3P)5s-3s^23p^4(3P)4p$
Argon II	434.81	19.4–16.64	$3s^23p^4(3P)4s-3s^23p^4(3P)4p$
Oxygen I	777.19	10.74–9.15	$2s^22p^3(^4S^\circ)3p-2s^22p^3(^4S^\circ)3s$
Oxygen I	844.62	10.99–9.52	$2s^22p^3(^4S^\circ)3p-2s^22p^3(^4S^\circ)3s$
Titanium I	318.65	3.89–0	$3d^3(^4F)4p-3d^24s^2$
Titanium I	363.52		$3d^2(^3F)4s4p(^1P^\circ)-3d^24s^2$
Titanium I	364.62	3.40–0	$3d^2(1D)4s4p(3P)-3d^24s^2$
Titanium I	375.29	3.35–0.047	$3d^2(^1D)4s4p(^3P)-3d^24s^2$
Titanium I	394.87	3.14–0	$3d^3(^4F)4p-3d^24s^2$
Titanium I	398.97	3.13–0.021	$3d^2(^3F)4s4p(^1P^\circ)-3d^24s^2$
Titanium I	429.11		
Titanium I	452.73	3.55–0.813	$3d^3(^4F)4p-3d^3(^4F)4s$
Titanium I	467.51	3.72–1.07	$3d^3(^4F)4p-3d^24s^2$
Titanium I	500.72	3.29–0.818	$3d^3(^4F)4p-3d^3(^4F)4s$
Titanium I	502.56		
Titanium I	506.21	4.61–2.16	$3d^3(a^2D)4p-3d^3(^2D^2)4s$
Titanium I	520.11	4.48–2.09	$3d^2(^3F)4s4p(^3P^*)-3d^24s(^4F)5s$
Titanium I	793.85	3.44–1.88	$3d^2(^3F)4s4p(^1P^*)-3d^3(^2G)4s$
Titanium II	263.86	8.54–3.84	$3d^2(^3F)4d-3d^2(^3F)4p$
Titanium II	274.65	8.38–3.87	$3d^2(^3F)4d-3d^2(^3F)4p$
Titanium II	282.13	8.06–3.66	$3d^2(^3F)4d-3d^2(^3F)4p$
Titanium II	295.2	8.06–3.86	$3d^2(^3F)4d-3d^2(^3F)4p$
Titanium II	308.14	7.74–3.72	$3d^2(^3F)5s-3d^2(^3F)4p$
Titanium II	322.94		
Titanium II	334.37	3.86–0.15	$3d^2(^3F)4p-3d^3$
Titanium II	348.36	7.87–4.31	$3d^2(^3F)5s-3d^2(^3F)4p$
Titanium II	454.4	3.97–1.24	$3d^2(^3F)4p-3d^2(^3P)4s$
Titanium II	465.72	3.90–1.24	$3d^2(^3F)4p-3d^2(^3P)4s$
Titanium II	518.59	4.28–1.89	$3d^2(^3F)4p-3d^2(^1G)4s$

about 15–20 °C higher than in a DC case. These facts show that the higher the thermal impact of plasma, the more inhomogeneous the temperature.

B. Optical emission spectroscopy (OES) analysis

Optical emission spectroscopy (OES) was used to analyze the emission footprint of our GFS plasma. The FloTron FT-X3 (Nova Fabrica Ltd., Lithuania) spectrometer with a 200, . . ., and 900 nm spectral range and 1.1 nm spectral resolution was used. Figure 13 shows how the optical probe unit was positioned inside the GFS system. An additional argon flow of 50 SCCM was used to save the optical window from deposition. In the Appendix, the raw OES spectra obtained for the Ti/Ar/O-plasma with (a) DC-power and (b) distance from nozzle variations are shown (Fig. 14). In all cases, the probing took place along the imaginable central line of a PJ. Comparing oxygen-free plasma with the one containing oxygen as a reactive gas [Fig. 14(a)], we detect the following differences: The excitation of argon ions and neutrals is suppressed in the presence of oxygen (compare spectra in the range of 730–780 nm for neutrals and 420 nm for ions). In contrast, Ti-neutrals get more excited in the presence of oxygen (450–520 nm region). We also detect excited TiO species and oxygen atoms resulting from secondary collision events. Since the main material of interest in this work is titania, we further concentrate on oxygen-containing plasma. Higher power leads to higher excitation of species and higher ionization intensity [Fig. 14(b)]. Excitation significantly declines with a backtrack from the target [Fig. 14(c)]. These results agree with the literature.[32–34]

The details of all emission lines found are given in Table I. The excitation energies for argon (>13.15 eV) and oxygen (>10.74 eV)

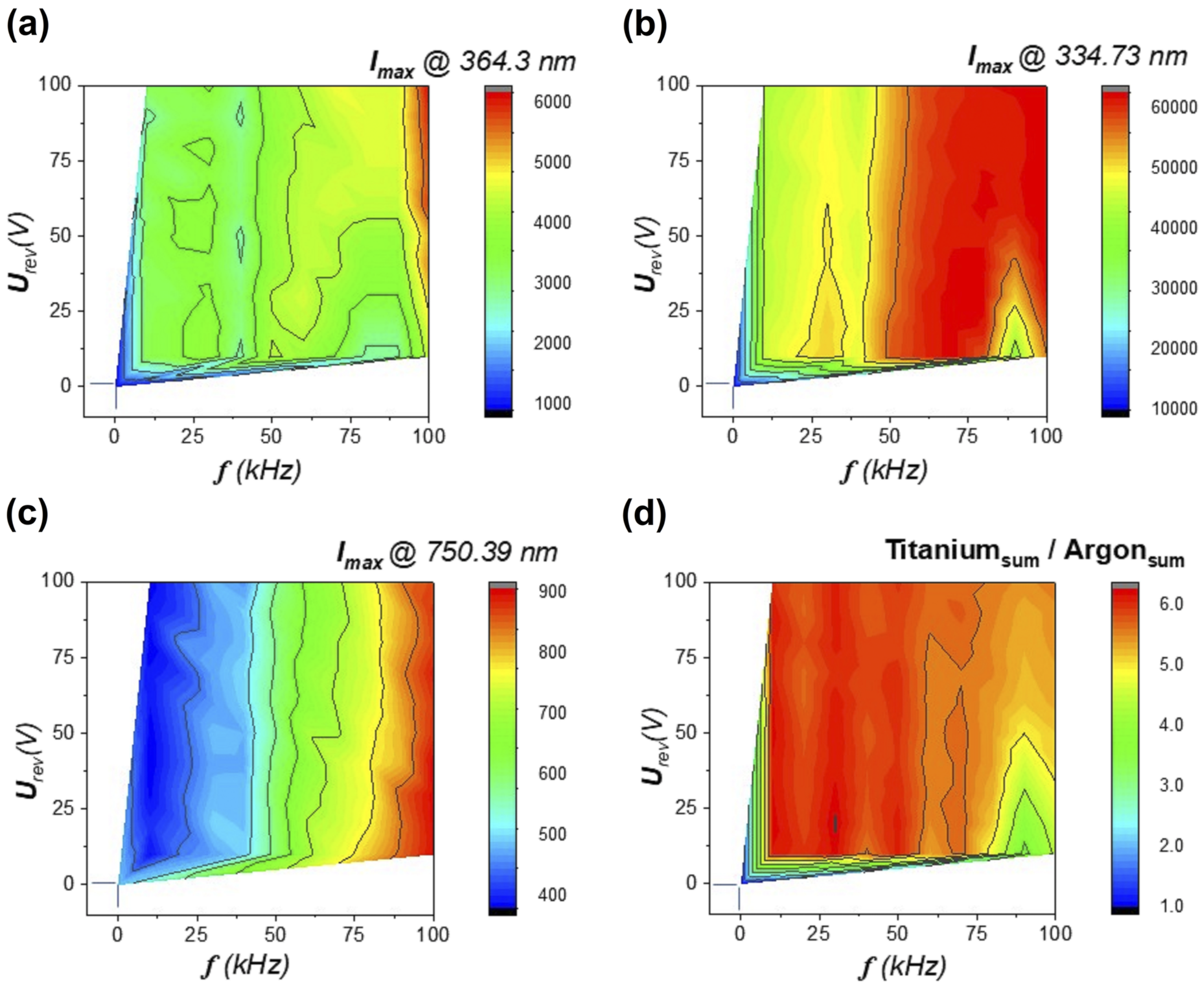

FIG. 4. 2D representation of plasma composition: Ti (a), Ti^+ (b), Ar (c), and Titanium to Argon ratio (d) depending on discharge regime. $Titanium_{sum}$ includes optically active Ti and Ti^+ species, and $Argon_{sum}$ includes Ar and Ar^+ species.

atoms are significantly higher than for titanium (>3.13 eV).[35,36] This explains why we detect mostly Ti-lines. The high ionization energy of Ar-atoms (15.76 eV) stipulates an even higher excitation energy for Ar^+ ions (>19.4 eV) that cannot be a pproached in conventional magnetron plasmas.[37] Ar-ions form in High-Power Impulse Magnetron Sputtering (HiPIMS, also known as HPPMS: High-Power Pulsed Magnetron Sputtering) processes because of the use of high-power pulses.[38]

The excitation of crucial species changes depending on f and U_{rev} parameters, as shown in Fig. 4. It is worth noticing that the main tendencies are preserved if just the intensities (the amplitudes but not the peak areas) of the main maxima for each optically active component are taken rather than the sum of all relevant peaks for the same. The intensities of the Ti, Ti^+, and Ar emission lines boost stepwise in the pulsed mode with increasing frequency. The same phenomenon was described by Britun *et al.*, where a strong emission intensity of Ti ion lines was observed in HiPIMS discharge compared to DC magnetron sputtering (DCMS).[39] The reverse voltage affects emission intensities negligibly.

IV. DEPOSITION OF TITANIA FILMS

Titania films have several electro-optic applications specified by the material properties, such as refractive index, density, phase composition, bandgap, conductivity, and others.[40–42] We follow in our development the concept of soft deposition of oxide layers, which means a low temperature of the substrate, low energy of species in a gas phase, and low UV irradiation approaching the substrate surface.

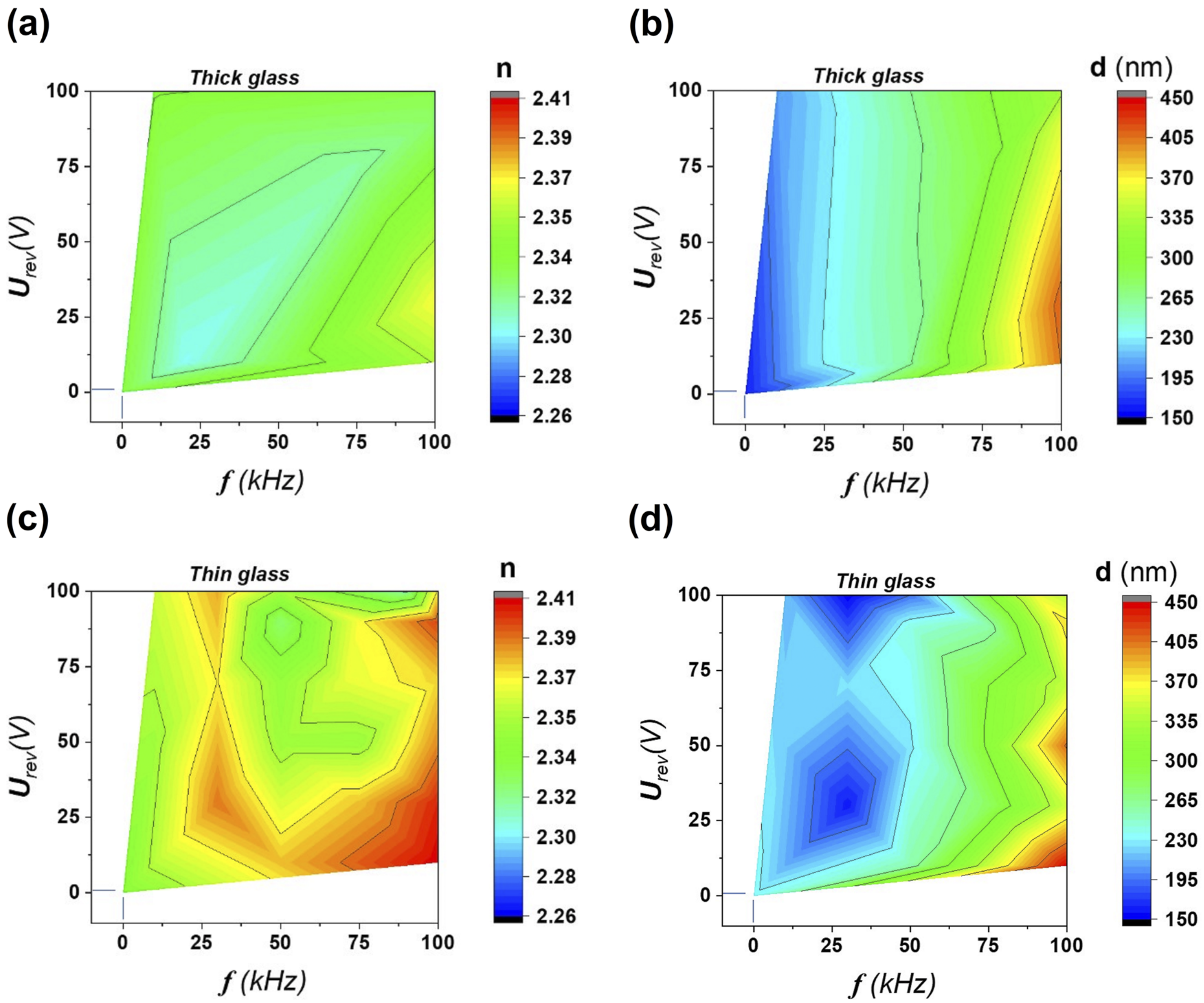

FIG. 5. Data of ellipsometry for GFS-TiO_x layers deposited without intentional heating on glass for 150 s. Thick glass (a) and (b) are compared with thin glass (c) and (d). Dependence of the real part of refractive index (a) and (c) and thickness (b) and (d).

TiO_2 thin films were deposited on glass substrates by the GFS hollow cathode, using Ar working gas and O_2 reactive gas. The Target is made of Titanium (purity 99, 99%). The glass substrates were cleaned with acetone and then dried with nitrogen gas before deposition.

Three phenomena and observations were presented: The dependency of deposition mode (DC and varied pulse), power, and oxygen flow. The deposition conditions, for titania films were as follows: q(Ar) = 1000 SCCM (standard cubic centimeter per minute), $q(O_2)$ = 80 SCCM, D_{st} = 1.5 cm, t_{dep} = 150 s, P = 500 W, DC the p_{tot} = 0.34 mbar, and no intentional heating. Eagle XG glass was used as a substrate.

To disclose how the optical properties of titania films change with plasma glowing conditions we used the Sentech Ellipsometer SE 850 (Sentech, Germany) with a μ-spot (which focuses the beam to 200 μm in diameter at the polarizer unit). The measurements were conducted at a fixed 70° incident angle in a spectral range of 280–850 nm. The spectra obtained were fit using SpecRay/3 software. A detailed description of the optical model used is given in the Appendix. Based on that, we obtained optical constants (refractive index n and extinction coefficient k) as well as layer thickness and an estimation of roughness (effective medium approximation). For films' comparison, we took those values at λ = 550 nm. X-ray diffraction (XRD) patterns were acquired in Bragg–Brentano geometry using the D8 Discover (Bruker AXS, Germany) instrument with Cu K_α radiation. A standard set of axial parallel plate collimators, 0.6 mm slits, and the LYNXEYE XE-T detector were used. Acquisition steps were 0.03°/5 s. The x-ray reflectometry (XRR) measurements were performed. On the same instrument, using Göbel-mirrors and slits, 0.2 mm primarily and 1 → 0.6 → 0.2 mm secondarily were applied for coupled scans with 0.01° and 2 s acquisition steps.

A. Influence of the pulsing parameters

As shown in Fig. 6, the titania layers' crystallinity depends on a pulsing regime. It is worth stressing that no intentional heating was used. As shown in Fig. 5 thick glass (a) and (b) are compared with thin glass (c) and (d). A dependence of the real parts of the refractive index (a) and (c) and thickness (b) and (d) on the pulsing conditions, frequency (f), and reverse voltage (U_{rev}) is presented.

Pulsing operations result in up to three times thicker titania layers as compared to DC ones. Generally, a distinctive increase in films' thickness was detected for both thin and thick glass when f increased. On the other hand, the refractive index remained almost unchanged in the case of thick glass and became higher in the case of thin glass substrates. This can be explained by a higher temperature in the latter case. The value of reverse voltage has no valuable influence on the film thickness, but it enlarges the refractive index of titania films.

The XRD results reveal some crystallinity in the films deposited onto thin glass only at the 100 kHz pulsing mode, regardless of the U_{rev} value (Fig. 6). Other titania films are x-ray amorphous. All titania films obtained on thick glass were found to be x-ray amorphous. These results, in combination with Fig. 3, give a crystallization temperature that lies between 350 and 400 °C. This is consistent with the results published elsewhere.[43]

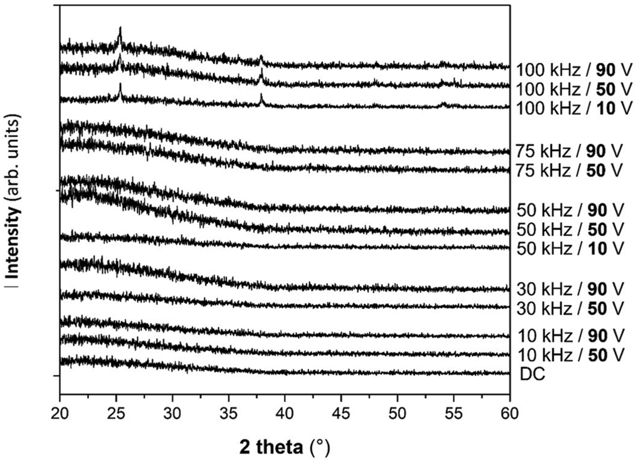

FIG. 6. XRD patterns obtained in symmetric scanning mode for the TiO_x films deposited at various pulsing conditions on thin glass. The following settings were fixed: 500 W, q(Ar) = 1000 SCCM, $q(O_2)$ = 80 SCCM, and t_{dep} = 150 s. The diffraction maxima exclusively correspond to the anatase phase.

The thermodynamic stability of rutile is higher than that of anatase. Nonetheless, in the pressure range of interest, the anatase-to-rutile reconstruction starts due to slow kinetics only at temperatures above 600 °C.[44] Without intentional heating, we do not reach this temperature.

The anatase phase is also known to form easily at high gas pressure during sputtering.[45] This is linked to the high deposition rate and reduced film density. This point will be considered below in more detail.

A comparison with Fig. 4 shows that the thermal impact of pulsing frequency is interrelated with the optical emission intensity of such species as Ti^*, Ti^+, and Ar^* (starlets point at excitation).

B. Influence of DC power

The influence of power on layer growth was investigated at different deposition powers. The ellipsometry results show that an increase in the applied power results in thicker layers with a higher refractive index (see Fig. 7). The refractive index is known to correlate with TiO_2 density.[46,47] Anatase reveals a lower refractive index (2.566 vs 2.742 at 550 nm)[48] and lower density (3.89 vs 4.23 g/cm^3) than rutile. Amorphous titania has even less n than anatase.[49]

Furthermore, oxygen stoichiometry also plays an important role. Thus, Ti_2O_3 and TiO have densities of 4.49 and 4.95 g/cm^3, respectively. Both oxides reveal, in direct comparison, higher refractive indices than stoichiometric TiO_2.[50] One may expect understoichiometric oxides to form in the face of oxygen shortages for reactive deposition processes. Particularly in the reactive deposition of TiO_x, $p(O_2)$ largely impacts the deposition rate and crystallization.[51]

Herewith, we used the XRR to estimate the density of the films in question. As shown in Fig. 16, the thicker the film gets, the smaller

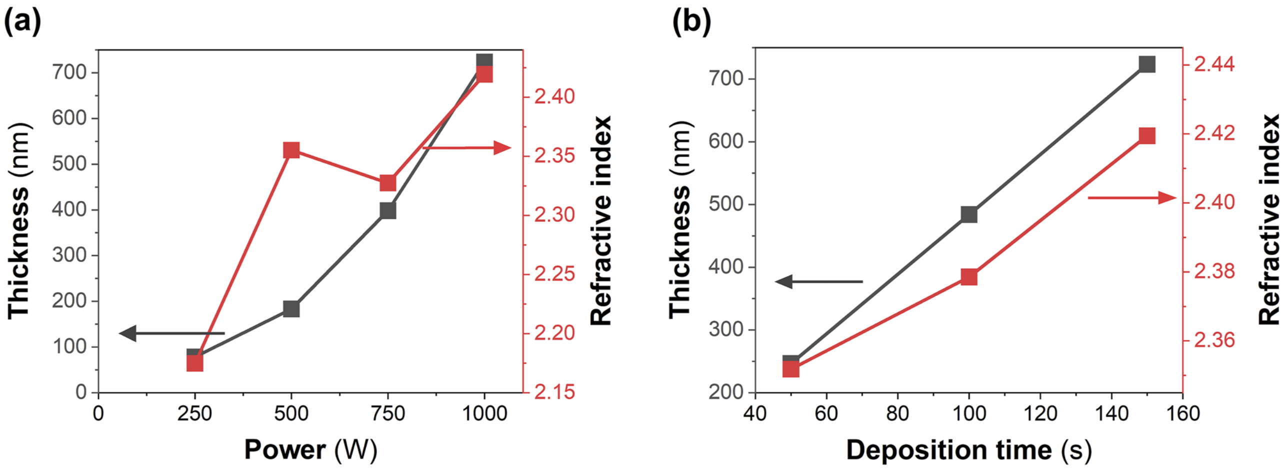

FIG. 7. Ellipsometry results: left, sum thickness of all three modeled layers; right, average weighted *n* for deposited samples with (a) 150 s with varied applied power and (b) 1000 W depositing power with different deposition times.

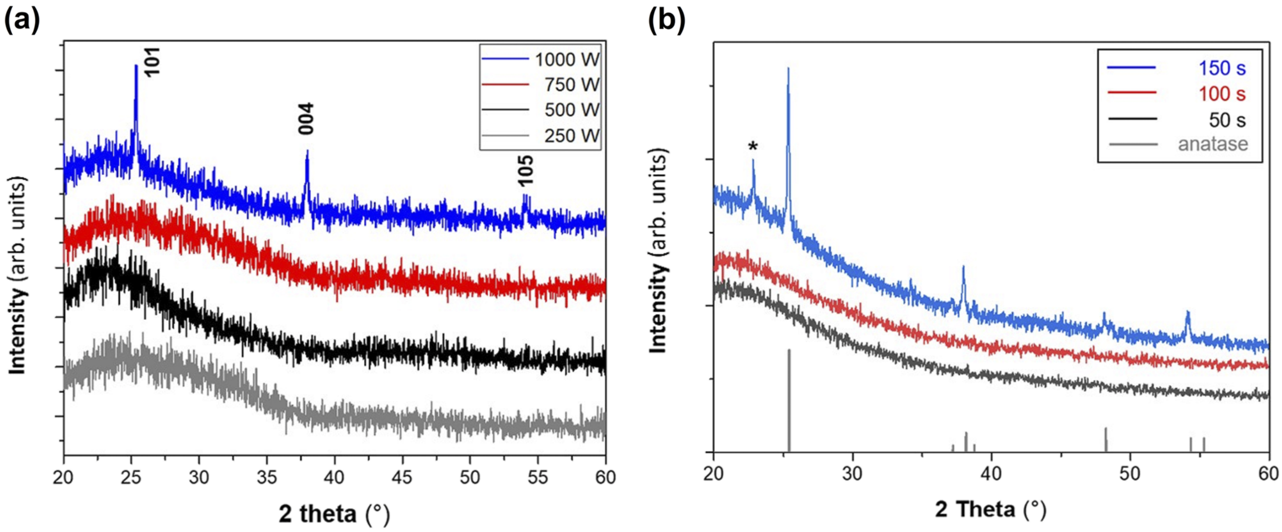

FIG. 8. XRD patterns obtained in symmetric scanning mode for the TiO_x films deposited in the DC regime with various power (a) and time (b). In the former case, deposition time was 150 s; in the latter case, power was 1000 W. In all cases, oxygen flow was 80 SCCM, and the target-to-substrate distance was 1.5 cm. The reflexes are ascribed to the anatase phase (PDF 01-070-6826). A starlet in (b) points to the possible presence of the under-stoichiometric Ti_6O_{11} phase (PDF 00-011-0454).

its density. Two thinner films are apparently oxygen deficient. The thickest film, which is crystalline [see Fig. 8(b)], shows a density lower than the theoretical one of anatase. That basically points to the presence of porosity. At the same time, the *n*-values slightly but continuously increase with increasing thickness [Fig. 7(b)]. This disagreement may only be explained by the insensitivity of ellipsometry to the kind of porosity that we have in our titania layers.[52] Indirectly, higher porosity in the very top layer of thicker TiO_x is reflected in larger roughness (Fig. 16) or effective medium approximation (EMA) thickness (Fig. 15). In fact, this phenomenon is common in sputtered films. Selectively, we detected for the films of comparable thickness a good correlation between XRR-density and refractive index.

The influence of power on the crystallinity of titania films is shown in Fig. 8(a). Only the crystalline anatase phase was detected in the films deposited at 1000 W power. Since the optimized optical model describing thick TiO_x films includes three layers (see Fig. 15), and this fact is supposedly related to the continuous heating

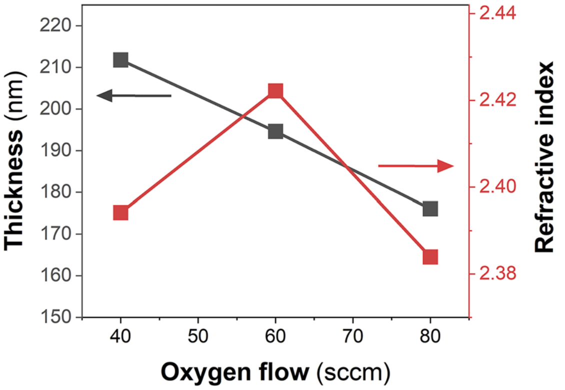

FIG. 9. Data of ellipsometry for the titania films deposited at different q(O_2). An entire layer's thickness is in relation to the average weighted refractive index (real part, *n*, determined at 550 nm) depicted.

of the substrate surface by plasma [see Fig. 12(a)], we also prepared and analyzed the deposition time (t_{dep}) series [Figs. 7(b) and 8(b)]. Increasing the deposition time results in thicker and denser layers.

We notice that the XRD patterns of the crystalline films from different series but deposited at the same conditions differ somewhat [compare Figs. 8(a) and 8(b)]. This phenomenon was observed more than once, and we suggest the boundary Ti/O stoichiometric conditions be the reason.

C. Influence of the oxygen stoichiometry

The influence of oxygen flow on layer properties was investigated for the crystalline films, which were obtained using 300 °C substrate heating, to secure a crystalline state of the films.

As follows from Fig. 9, higher oxygen content in the gas phase led to thinner films. It means that the deposition rate decreases with q(O_2). This trend may be explained by the formation of Ti–O species in a gas phase, which reveals, in turn, poorer diffusion to the substrate surface than single atoms or ions. They are finally eliminated to a large extent by the gas flow. The refractive index depends mostly on crystallinity, layer density, and stoichiometry. They are all generally related to the deposition temperature.[53] The maximum refractive index is known to increase in value with oxygen content in TiO_x films; however, its position shifts along the wavelength axis in an unsystematic way.[54] It means that at a fixed wavelength, we may detect both an increase and a decrease of the *n* with oxygen. Therefore, the decrease of *n* at higher q(O_2) is most probably related to the shift of its maximum to another wavelength.

The XRD patterns of titania films deposited with variable reactive oxygen flow and the corresponding plane view of the samples are shown in Fig. 10. Low q(O_2) results in nonhomogeneous films with a dark bluish fleck in the middle. The measurements were performed exactly in the middle, and a phase analysis on the larger 2θ-range revealed no presence of metallic titanium. It does not necessarily exclude the occurrence of a metallic phase; however, a detected shift of the (101)-diffraction maximum toward a larger 2θ-angle coinciding with the disappearance of the darker middle area in the film rather points at a changing oxygen stoichiometry in TiO_x. Indeed, even the low content of Ti^{3+} ions in titania may cause such a coloration.[55]

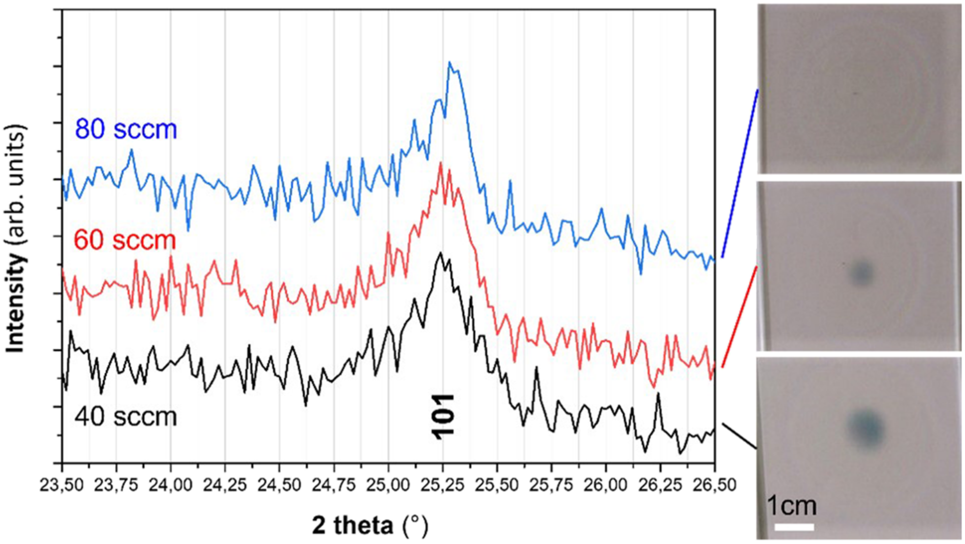

FIG. 10. XRD patterns obtained in symmetric scanning mode for the TiO_x films deposited in the DC regime with various oxygen flows were noticed. In all cases, q(Ar), power, and D_{t-s} were 1000 SCCM, 500 W, and 1.5 cm, respectively. The (101)-peak corresponds to the anatase phase (PDF 01-070-6826). The corresponding photographs of the samples on glass are also shown.

V. CONCLUSIONS

The lab GFS system with the reverse (positive) pulsing voltage supply is described in detail. The deposition method is evaluated using the example of Titania films. A comprehensive set of experimental data characterizing plasma conditions in relation to the film's properties is presented. The thermal impact of GFS plasma was found to be dependent on pulsing parameters. The pulsing frequency (*f*) is a significant factor that provides additional substrate heating by ~100 °C when the plasma regime changes from $f = 0$ (DC) to 100 kHz. Such a change in frequency provides a significant steady increase in the OES signals of Ti and Ar neutrals as well as Ti^+ ions. GFS plasma may be used to heat the substrate surface to more than 400 °C within several minutes. As a result of this impact, crystalline anatase TiO_x films can be deposited without intentional heating. To reach crystallization temperature, either power in DC mode or pulsing frequency at a fixed power should be increased. Such significant warming of the substrate surface during deposition stipulates a steadily changing microstructure across the film thickness. This interrelates with the drift in optical properties, density, and crystallinity. Only the top layer gets crystallized if no intentional heating is used. Since the deposition rate in a DC mode is lower than in a pulsing one, the highest density and refractive index can be reached when the intentional heating and DC deposition modes are combined.

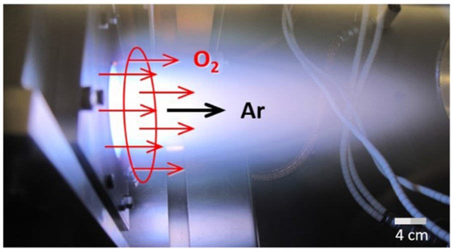

FIG. 11. Photo of the glowing GFS-PJ with the marked gas fluxes. The conditions are DC 500 W, q(Ar) = 1000 SCCM, and $q(O_2)$ = 80 SCCM.

ACKNOWLEDGMENTS

This work was supported by the State Government of Berlin (SENBWF) in the frame of the Program "Spitzenforschung und Innovation in den Neuen Ländern" (Grant No. 03IS2151E). Financial support was also provided by the German Federal Ministry for Economic Affairs and Energy (project TCO4CIGS, Contract No. 0325762).

AUTHOR DECLARATIONS

Conflict of Interest

The authors have no conflicts to disclose.

Author Contributions

Nivin Alktash: Conceptualization (supporting); Data curation (lead); Formal analysis (lead); Investigation (lead); Methodology (lead); Validation (supporting); Visualization (lead); Writing – original draft (lead); Writing – review & editing (supporting). **Ruslan Muydinov**: Conceptualization (lead); Data curation (supporting); Formal analysis (supporting); Investigation (supporting); Methodology (supporting); Supervision (equal); Validation (lead); Visualization (supporting); Writing – original draft (supporting); Writing – review & editing (lead). **Darja Erfurt**: Investigation (supporting). **Manuel Hartig**: Investigation (supporting). **Wojciech Gajewski**: Investigation (supporting); Resources (supporting); Visualization (supporting). **Bernd Szyszka**: Conceptualization (supporting); Funding acquisition (lead); Project administration (lead); Resources (lead); Supervision (equal); Validation (supporting); Writing – review & editing (supporting).

DATA AVAILABILITY

The data that support the findings of this study are available from the corresponding author upon reasonable request.

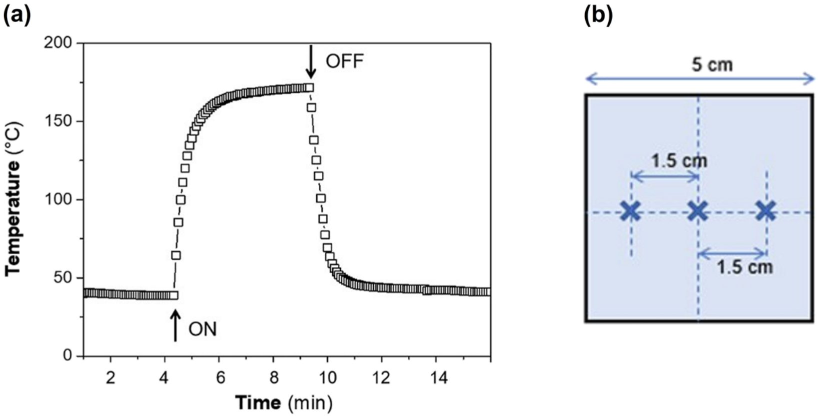

FIG. 12. (a) Typical temperature measurement curve. The arrows point at switching the GFS plasma on and off. (b) Measurement positions shown with crosses on the 5 × 5 cm^2 glass substrate.

APPENDIX: SUPPORTING INFORMATION

Fitting the S_1/S_2 spectra obtained for the thick titania films disclosed the necessity of using a multilayer model to minimize the mean square error (MSE).

The film's microstructure changes when it gets thicker (Fig. 15). This phenomenon originates from the strong heating effect of plasma, which especially develops within the first few minutes [Fig. 12(a)]. Table II illustrates how the MSE values differ for 2-layer (2L) and 3-layer (3L) optical models describing titania films of several hundreds of nanometers in thickness.

As one may see, the higher the substrate temperature, the more the 3L model has been applied to all titania films analyzed in this work.

A Bruggman effective medium approximation (EMA)[60] containing 50% of a dense TiO_x (Brendel model) and 50% of the air was used to model the surface roughness.

TABLE II. Comparison of the optical models in terms of MSE for different deposition conditions.

Deposition regime	2L	3L
DC, no heating	~8	~5
MF, no heating	~9–10	~6
DC, T_s = 300 °C	~27–30	~6–7

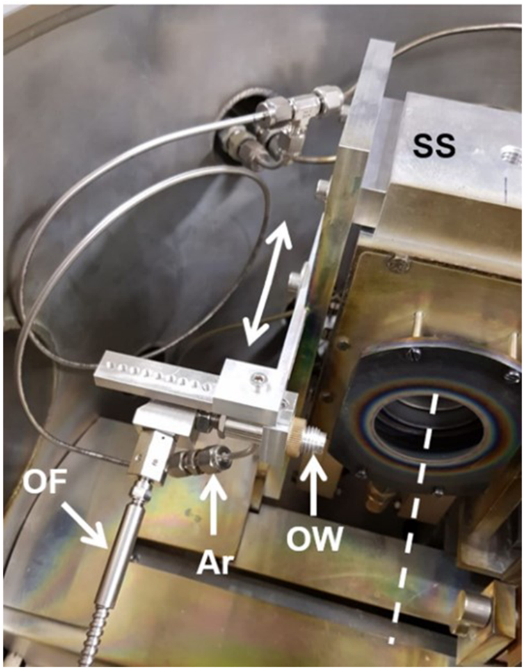

FIG. 13. Optical probe construction for the GFS plasma analysis: SS—sputter source; OF—optical fiber with vacuum throughput; OW—optical window; and Ar—argon gas supply for shielding. The dashed line shows the axial center of the SS and plasma jet, and parallel to it, a double-sided arrow shows the linear degree of freedom for the probe fixation.

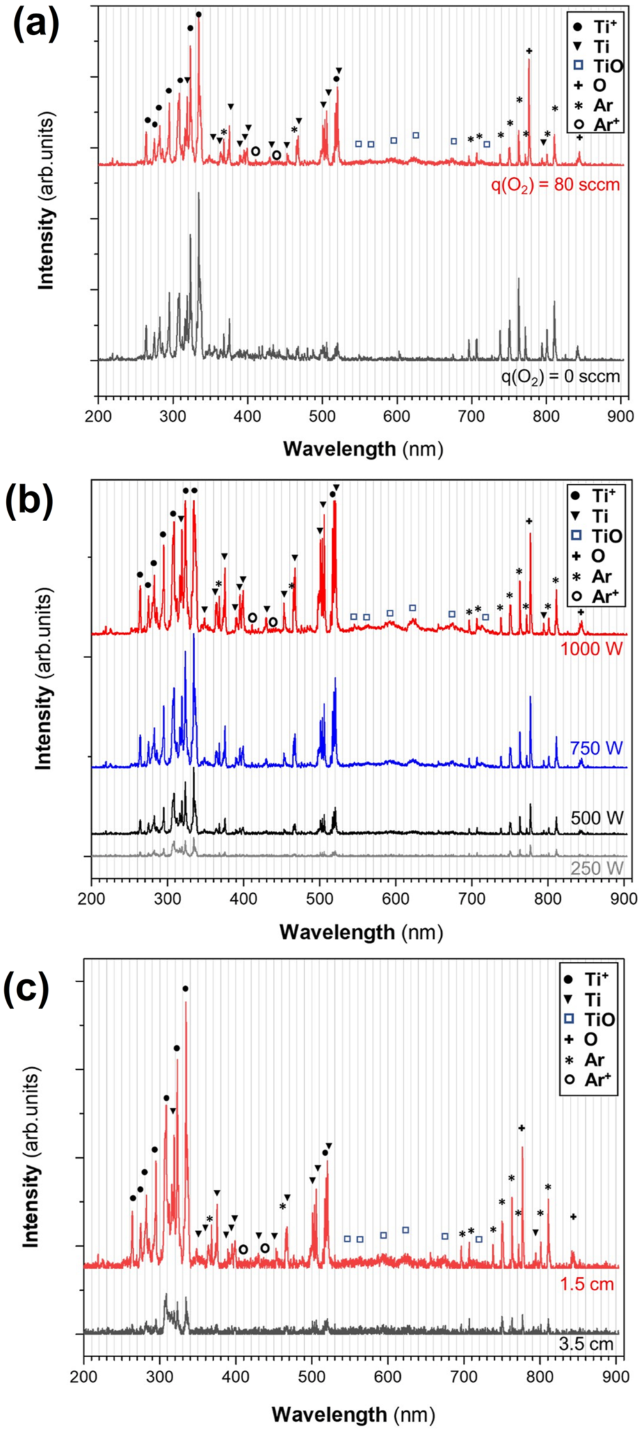

FIG. 14. Optical emission spectra of the Ar/Ti plasma at different conditions. (a) Impact of oxygen reactive gas at a 1.5 cm distance from the source and 500 W discharge power. (b) Effect of power on reactive plasma composition. (c) The difference in reactive plasma composition [q(Ar) = 1000 SCCM and $q(O_2)$ = 80 SCCM] between 1.5 and 3.0 cm distances from the source. In all cases, a DC-discharge regime was used. The attribution of characteristic emission maxima was based on the literature data.[56–59]

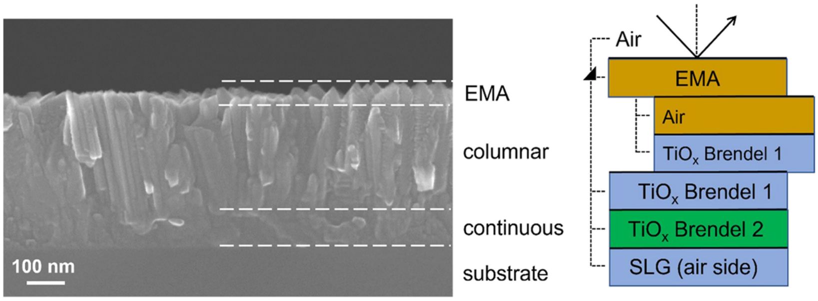

FIG. 15. SEM cross-section image of the titania film deposited at 500 W, 100 kHz, 50 V, 2 μs, and 150 s on a Si wafer without external heating. On the right is a corresponding graphical representation of the triple layer (3L) model, which was used for fitting the corresponding ellipsometry spectrum in SpectraRay. A 2L model would include one dense Brendel layer and one EMA layer.

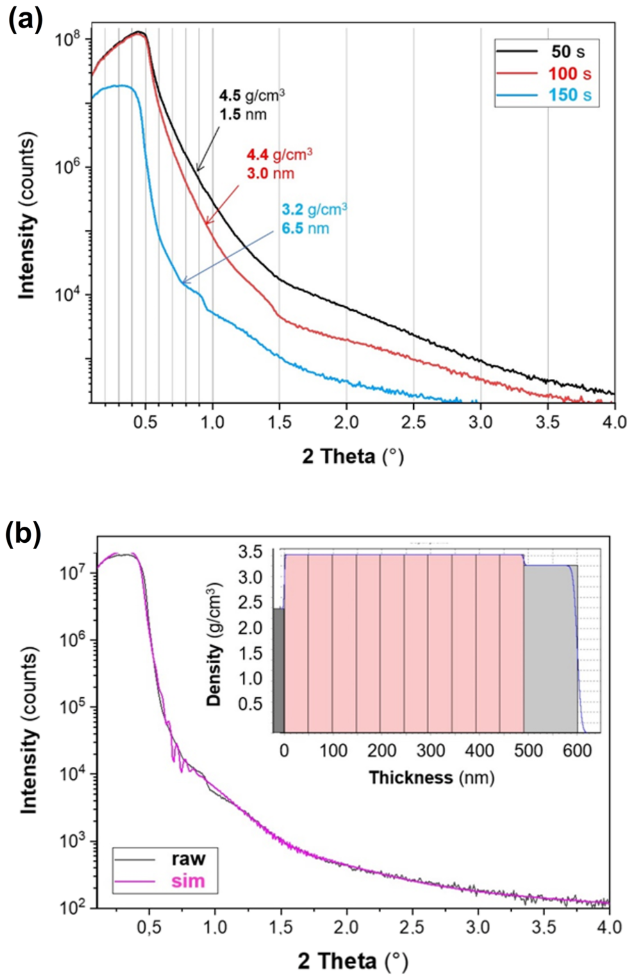

FIG. 16. XRR results for the titania films deposited with various deposition times (a). The films are the same as those presented in Fig. 7(b). (b) A fitting result for the thickest film (150 s deposition time), where "raw" presents the measured curve and "sim" presents the simulated one. The inset shows the density profile, where the glass substrate is shown in gray and two contributions to the titania layer—in light magenta and light gray colors. Thinner films in (a) were simulated with a single contribution.

The Brendel-oscillator model was used to model a bulk part of the film (as shown in Fig. 15) in the middle-infrared (MIR) range. It is based on a harmonic oscillator model and describes the standard deviation of the Gaussian distribution of the center frequency of the harmonic oscillator. The complex dielectric function $\varepsilon(\nu)$ can be expressed in the following forms:

$$\boldsymbol{\varepsilon}(\boldsymbol{\nu}) = \boldsymbol{\varepsilon}_\infty + \sum_{k=1}^{m} \boldsymbol{x}_k(\boldsymbol{\nu}), \tag{A1}$$

$$\boldsymbol{x}_k(\boldsymbol{\nu}) = \frac{1}{\boldsymbol{\sigma}_k\sqrt{2\pi}} \int_{-\infty}^{+\infty} \exp\left(-\frac{(\boldsymbol{x}-\boldsymbol{\nu}_{ok})^2}{2\boldsymbol{\sigma}^2}\right) * \frac{\boldsymbol{\nu}_{pk}^2}{\boldsymbol{x}^2-\boldsymbol{\nu}^2-\boldsymbol{i}\boldsymbol{\nu}_{Tk}\boldsymbol{\nu}}, \tag{A2}$$

where $\boldsymbol{x}_k$ is the susceptibility of the Brendel oscillator k, $\boldsymbol{\nu}_{ok}$ is the resonance frequency, $\boldsymbol{\nu}_{Tk}$ is the damping of the oscillator, $\boldsymbol{\nu}_{pk}$ is the oscillator strength, $\boldsymbol{\sigma}_k$ is the standard deviation of the center frequency, and k is the oscillator index.[61–63]

The following relationships determine the refractive index n and extinction coefficient k, which represent the real and imaginary parts of the complex refractive index ($\boldsymbol{N}^* = \boldsymbol{n} - \boldsymbol{ik}$),[61–63]

$$\boldsymbol{n} = \frac{1}{\sqrt{2}}\sqrt{\sqrt{\boldsymbol{\varepsilon}_1^2+\boldsymbol{\varepsilon}_2^2}+\boldsymbol{\varepsilon}_1}, \tag{A3}$$

$$\boldsymbol{k} = \frac{1}{\sqrt{2}}\sqrt{\sqrt{\boldsymbol{\varepsilon}_1^2+\boldsymbol{\varepsilon}_2^2}-\boldsymbol{\varepsilon}_1}. \tag{A4}$$

The refractive index $\boldsymbol{n}_{\mathbf{weighted}}$ represented in the paper was calculated from the following relationship:

$$\boldsymbol{n}_{\mathbf{weighted}} = \frac{\boldsymbol{n}_1\mathrm{d}_1+\boldsymbol{n}_2\mathrm{d}_2+\boldsymbol{n}_3\mathrm{d}_3}{\boldsymbol{d}_1+\mathrm{d}2+\boldsymbol{d}_3}. \tag{A5}$$

REFERENCES

[1] F. Paschen, "Bohrs heliumlinien," Ann. Phys. **355**(16), 901–940 (1916).
[2] A. D. White, "New hollow cathode glow discharge," J. Appl. Phys. **30**(5), 711–719 (1959).

[3] *Physics and Applications of Pseudosparks*, edited by M. A. Gundersen and G. Schaefer (Springer, Boston, MA, 1990), Vol. 219.

[4] S. Muhl and A. Pérez, "The use of hollow cathodes in deposition processes: A critical review," Thin Solid Films **579**, 174–198 (2015).

[5] H. Sakuma and K. Ishii, "Gas flow sputtering: Versatile process for the growth of nanopillars, nanoparticles, and epitaxial thin films," J. Magn. Magn. Mater. **321**(7), 872–875 (2009).

[6] See https://cordis.europa.eu/project/id/275599/reporting/de for final report summary–NANOHAP (nanocomposite approaches for the deposition of highly active photocatalytic thin films with plasma technology)|FP7|CORDIS|European Commission (europa.eu).

[7] F. Jiang *et al.*, "A two-terminal perovskite/perovskite tandem solar cell," J. Mater. Chem. A **4**(4), 1208–1213 (2016).

[8] A. Wiatrowski *et al.*, "Comparison of the physicochemical properties of TiO_2 thin films obtained by magnetron sputtering with continuous and pulsed gas flow," Coatings **8**(11), 412 (2018).

[9] S. Rtimi, O. Baghriche, C. Pulgarin, J.-C. Lavanchy, and J. Kiwi, "Growth of TiO_2/Cu films by HiPIMS for accelerated bacterial loss of viability," Surf. Coat. Technol. **232**, 804–813 (2013).

[10] O.-G. Simionescu, C. Romanițan, O. Tutunaru, V. Ion, O. Buiu, and A. Avram, "RF magnetron sputtering deposition of TiO_2 thin films in a small continuous oxygen flow rate," Coatings **9**(7), 442 (2019).

[11] Y. Kubo, Y. Iwabuchi, M. Yoshikawa, Y. Sato, and Y. Shigesato, "High rate deposition of photocatalytic TiO_2 films with high activity by hollow cathode gas-flow sputtering method," J. Vac. Sci. Technol. A **26**(4), 893 (2008).

[12] T. Koida, H. Fujiwara, and M. Kondo, "Hydrogen-doped In_2O_3 as high-mobility transparent conductive oxide," Jpn. J. Appl. Phys. **46**(7L), L685–L687 (2007).

[13] D. P. Howard, P. Marchand, C. J. Carmalt, I. P. Parkin, and J. A. Darr, "Si-doped zinc oxide transparent conducting oxides; nanoparticle optimisation, scale-up and thin film deposition," J. Mater. Chem. C **5**(34), 8796–8801 (2017).

[14] L. Vivar Mora, S. Naik, S. Paul, R. Dawson, A. Neville, and R. Barker, "Influence of silica nanoparticles on corrosion resistance of sol-gel based coatings on mild steel," Surf. Coat. Technol. **324**, 368–375 (2017).

[15] D. Borisova, H. Möhwald, and D. G. Shchukin, "Mesoporous silica nanoparticles for active corrosion protection," ACS Nano **5**(3), 1939–1946 (2011).

[16] D. Koeßler, K. Ortner, M. Höfer, B. Szyszka, and T. Jung, "Preparation of photocatalytic TiO_2-coatings by hollow cathode gas-flow sputtering," in Proceedings of the 8th International Conference on Coatings on Glass and Plastics ICCG Braunschweig, Germany, 13–17 June (2010).

[17] See http://www.ghs-gmbh.com/ for GHS Prozessautomation GmbH.

[18] Process field bus–standard communication in automation technology, promoted in 1989.

[19] T. Kälber, *Hohlkathoden-Gasflußsputtern zur Verschleißschutzbeschichtung von Kunststoffen* (Fraunhofer IRB Verl, Stuttgart, 1998).

[20] L. Bárdoš, H. Baránková, and S. Berg, "Thin film processing by radio frequency hollow cathodes," Surf. Coat. Technol. **97**(1–3), 723–728 (1997).

[21] C. Paduraru, K. H. Becker, A. Belkind, J. L. Lopez, and Y. Aranda Gonzalvo, "Characterization of the remote plasma generated in a pulsed-DC gas-flow hollow-cathode discharge," IEEE Trans. Plasma Sci. **35**(3), 527–533 (2007).

[22] See https://www.coolermaster.com/catalog/coolers/thermal-grease/ic-value-v1/#specifications for information about fixing thermal Grease.

[23] X. Li, B. Bakhit, M. P. J. Jõesaar, L. Hultman, I. Petrov, and G. Greczynski, "Toward energy-efficient physical vapor deposition: Routes for replacing substrate heating during magnetron sputter deposition by employing metal ion irradiation," Surf. Coat. Technol. **415**, 127120 (2021).

[24] Mahan2000_physical vapor deposition of thin films.pdf.

[25] H. Kersten, H. Deutsch, H. Steffen, G. M. W. Kroesen, and R. Hippler, "The energy balance at substrate surfaces during plasma processing," Vacuum **63**(3), 385–431 (2001).

[26] J. A. Thornton, "Substrate heating in cylindrical magnetron sputtering sources," Thin Solid Films **54**(1), 23–31 (1978).

[27] J. A. Thornton and J. L. Lamb, "Substrate heating rates for planar and cylindrical-post magnetron sputtering sources," Thin Solid Films **119**(1), 87–95 (1984).

[28] R. Wendt, K. Ellmer, and K. Wiesemann, "Thermal power at a substrate during ZnO:Al thin film deposition in a planar magnetron sputtering system," J. Appl. Phys. **82**(5), 2115–2122 (1997).

[29] V. Bhatt and S. Chandra, "Silicon nitride films deposited by RF sputtering for microstructure fabrication in MEMS," J. Electron. Mater. **38**(9), 1979–1989 (2009).

[30] M. Andritschky, F. Guimarães, and V. Teixeira, "Energy deposition and substrate heating during magnetron sputtering," Vacuum **44**(8), 809–813 (1993).

[31] J. Krishnasamy, K. Y. Chan, and T. Y. Tou, "Influence of process parameters on the substrate heating in direct current plasma magnetron sputtering deposition process," Microelectron. Int. **27**(2), 75–78 (2010).

[32] G. S. Chen, C. C. Lee, H. Niu, W. Huang, R. Jann, and T. Schütte, "Sputter deposition of titanium monoxide and dioxide thin films with controlled properties using optical emission spectroscopy," Thin Solid Films **516**(23), 8473–8478 (2008).

[33] C. Nouvellon *et al.*, "Emission spectrometry diagnostic of sputtered titanium in magnetron amplified discharges," J. Appl. Phys. **92**(1), 32–36 (2002).

[34] N. Britun, M. Gaillard, L. Schwaederlé, Y. M. Kim, and J. G. Han, "Spatial characterization of Ar–Ti plasma in a magnetron sputtering system using emission and absorption spectroscopy," Plasma Sources Sci. Technol. **15**(4), 790–796 (2006).

[35] A. Belkind, W. Zhu, J. Lopez, and K. Becker, "Time-resolved optical emission spectroscopy during pulsed dc magnetron sputter deposition of Ti and TiO_2 thin films," Plasma Sources Sci. Technol. **15**(2), S17–S25 (2006).

[36] S. Konstantinidis, F. Gaboriau, M. Gaillard, M. Hecq, and A. Ricard, "Optical plasma diagnostics during reactive magnetron sputtering," in *Reactive Sputter Deposition*, edited by D. Depla and S. Mahieu (Springer, Berlin, Heidelberg, 2008), Vol. 109, pp. 301–335.

[37] A. Belkind, A. Freilich, J. Lopez, Z. Zhao, W. Zhu, and K. Becker, "Characterization of pulsed dc magnetron sputtering plasmas," New J. Phys. **7**, 90 (2005).

[38] N. Britun, S. Konstantinidis, A. Belosludtsev, T. Silva, and R. Snyders, "Quantification of the hysteresis and related phenomena in reactive HiPIMS discharges," J. Appl. Phys. **121**(17), 171905 (2017).

[39] N. Britun, S. Konstantinidis, and R. Snyders, "Diagnostics of magnetron sputtering discharges by resonant absorption spectroscopy," in *Plasma Science and Technology: Progress in Physical States and Chemical Reactions*, edited by T. Mieno (InTech, 2016).

[40] D. C. Cronemeyer, "Electrical and optical properties of rutile single crystals," Phys. Rev. **87**(5), 876–886 (1952).

[41] O. Carp, "Photoinduced reactivity of titanium dioxide," Prog. Solid State Chem. **32**(1–2), 33–177 (2004).

[42] M. Kitui, M. M. Mwamburi, F. Gaitho, and C. M. Maghanga, "Optical properties of TiO_2 based multilayer thin films: Application to optical filters," Int. J. Thin Films Sci. Technol. **4**, 17 (2015).

[43] O. Durante *et al.*, "Emergence and evolution of crystallization in TiO_2 thin films: A structural and morphological study," Nanomaterials **11**(6), 1409 (2021).

[44] D. A. H. Hanaor and C. C. Sorrell, "Review of the anatase to rutile phase transformation," J. Mater. Sci. **46**(4), 855–874 (2011).

[45] H. Kotake, J. Jia, S.-i. Nakamura, T. Okajima, and Y. Shigesato, "Tailoring the crystal structure of TiO_2 thin films from the anatase to rutile phase," J. Vac. Sci. Technol. A **33**(4), 041505 (2015).

[46] C. H. Huang, C. C. Tsao, and C. Y. Hsu, "Study on the photocatalytic activities of TiO_2 films prepared by reactive RF sputtering," Ceram. Int. **37**(7), 2781–2788 (2011).

[47] D. Mergel, D. Buschendorf, S. Eggert, R. Grammes, and B. Samset, "Density and refractive index of TiO_2 films prepared by reactive evaporation," Thin Solid Films **371**(1–2), 218–224 (2000).

[48] A. Matthias, N. Raićevic, R. Donfeu Tchana, D. Kip, and J. Deubener, "Density dependence of refractive index of nanoparticle-derived titania films on glass," Thin Solid Films **558**, 86–92 (2014).

[49] A. Bendavid and P. J. Martin, "Review of thin film materials deposition by the filtered cathodic vacuum arc process at CSIRO," J. Aust. Ceram. Soc. **50**, 86–101 (2014).

[50] H. K. Pulker, G. Paesold, and E. Ritter, "Refractive indices of TiO_2 films produced by reactive evaporation of various titanium–oxygen phases," Appl. Opt. **15**(12), 2986 (1976).

[51] H. Toku, R. S. Pessoa, H. S. Maciel, M. Massi, and U. A. Mengui, "The effect of oxygen concentration on the low temperature deposition of TiO_2 thin films," Surf. Coat. Technol. **202**(10), 2126–2131 (2008).

[52] M. M. Abdel-Aziz, I. S. Yahia, L. A. Wahab, M. Fadel, and M. A. Afifi, "Determination and analysis of dispersive optical constant of TiO_2 and Ti_2O_3 thin films," Appl. Surf. Sci. **252**(23), 8163–8170 (2006).

[53] P. K. Manoj, P. Koshy, and V. K. Vaidyan, "Transparent anatase titania films: A critical study on optical properties," Prog. Nat. Sci.: Mater. Int. **22**(2), 79–85 (2012).

[54] A. S. Hassanien and A. A. Akl, "Optical characterizations and refractive index dispersion parameters of annealed TiO_2 thin films synthesized by RF-sputtering technique at different flow rates of the reactive oxygen gas," Physica B **576**, 411718 (2020).

[55] L.-B. Xiong, J.-L. Li, B. Yang, and Y. Yu, "Ti^{3+} in the surface of titanium dioxide: Generation, properties and photocatalytic application," J. Nanomater. **2012**, 831524.

[56] K. S. Mogensen *et al.*, "Optical emission spectroscopy on pulsed-DC plasmas used for TiN depositions," Surf. Coatings Technol. **102**(1–2), 41–49 (1998).

[57] S. Y. Guo, W. N. Shafarman, and A. E. Delahoy, "TiN and TiO_2: Nb thin film preparation using hollow cathode sputtering with application to solar cells," J. Vac. Sci. Technol. A **24**(4), 1524 (2006).

[58] M. J. Jung, K. H. Nam, L. R. Shaginyan, and J. G. Han, "Deposition of Ti thin film using the magnetron sputtering method," Thin Solid Films **435**(1–2), 145–149 (2003).

[59] T. Welzel, "Plasmadiagnostische charakterisierung der magnetronentladung zur c-BN-abscheidung," Ph.D. thesis, TU Chemnitz, 1998, p. 120.

[60] D. A. G. Bruggeman, "Berechnung verschiedener physikalischer Konstanten von heterogenen Substanzen. I. Dielektrizitätskonstanten und Leitfähigkeiten der Mischkörper aus isotropen Substanzen," Ann. Phys. **416**(7), 636–664 (1935).

[61] R. Brendel and D. Bormann, "An infrared dielectric function model for amorphous solids," J. Appl. Phys. **71**(1), 1–6 (1992).

[62] U. Richter, G. Dittmar, and H. Ketelsen, SENTECH SpectraRay/3 software manual, 2013, pp. 266–267.

[63] M. Horprathum, P. Chindaudom, and P. Limsuwan, "A spectroscopic ellipsometry study of TiO_2 thin films prepared by dc reactive magnetron sputtering: Annealing temperature effect," Chin. Phys. Lett. **24**(6), 1505–1508 (2007).